

Measurement of the neutrino-oxygen neutral-current quasielastic cross section using atmospheric neutrinos in the SK-Gd experiment

Graduate School of Natural Science and Technology
Okayama University

Seiya Sakai

March 1, 2024

ABSTRACT

Neutrino is neutrino.
Don't you know neutrino?

ACKNOWLEDGMENTS

Thank you so much!

Contents

1	Introduction	1
1.1	Neutrino	1
1.2	Neutrino oscillation	1
1.3	Supernova explosion	2
1.4	Current status of DSNB search	2
1.5	Neutrino-oxygen NCQE reactions	2
2	Super-Kamiokande	7
2.1	Super-Kamiokande	7
2.2	ID PMT and OD PMT	8
2.3	Helmholtz coils	11
2.4	Observation phase	11
2.5	Detection principle	13
2.6	Water purification system	14
2.7	Air purification system	15
2.8	Data acquisition system	17
3	Calibration	19
3.1	ID detector calibration	19
4	Simulation	23
4.1	Atmospheric neutrino flux	23
4.2	Neutrino interaction	23
4.3	Simulation for the IBD-like event	23
4.4	Detector simulation	23
5	Event reconstruction	26
5.1	Reconstructed Cherenkov angle of prompt signal	26
6	Event reduction	27
6.1	First reduction	27
6.2	Second reduction: spallation cut	27
6.3	Third reduction	27
6.4	Fourth reduction: neutron tagging	27
7	Comparison of secondary interaction models	28
7.1	Secondary interaction models	28
8	NCQE cross section measurement	29
8.1	NCQE cross section measurement	29
9	Results	30
9.1	measured NCQE cross section	30

10 Conclusion	31
A Neutrino oscillation between two neutrino species in vacuum	32

List of Figures

1.1	Time evolution of the luminosity and average energy of neutrinos	3
1.2	Events from SN1987A observed in Kamiokande-II and the IMB detector	3
1.3	Schematic view of the DSNB event	3
1.4	Predictions of DSNB $\bar{\nu}_e$ flux from various theoretical models	4
1.5	Effective neutrino interaction cross sections including energy resolution and threshold effects in large water Cherenkov detectors	4
1.6	Upper limit of the $\bar{\nu}_e$ flux in the SK-Gd DSNB search	5
1.7	Schematic view of the DSNB and NCQE events	5
1.8	Schematic view of the NCQE event	6
2.1	Overview of the Super-Kamiokande detector	7
2.2	Cross section of the SK detector and overview of supermodule frames	8
2.3	Schematic view of the ID PMT	9
2.4	Quantum efficiency of the ID PMT photocathode as a function of wavelength	9
2.5	Single photoelectron pulse height distribution of the ID PMT	9
2.6	Relative transit time distribution for a typical ID PMT tested using 410 nm wavelength light at the single photoelectron intensity level	10
2.7	Positional relationship of ID PMTs and OD PMTs in a supermodule frame	10
2.8	Schematic view of Helmholtz coils	11
2.9	Picture of a shockwave prevention case	12
2.10	Schematic view of Cherenkov radiation	14
2.11	Schematic view of water purification system	15
2.12	Typical radon concentration in the air at the SK over a year	16
2.13	Schematic view of air purification system	16
2.14	Schematic view of the data acquisition system	18
2.15	Block diagram of the QTC and its surroundings	18
3.1	Location of standard PMTs in ID and schematic view of the groups of PMTs	19
3.2	Picture of the Ni-Cf source	19
3.3	Single-pe distribution of the Ni-Cf source data in SK-III	20
3.4	Schematic view of the timing calibration system and cross section of the diffuser ball	20
3.5	Timing and charge distribution for a readout channel	21
3.6	Schematic view of the laser calibration system and TOF-subtracted timing distributions of the laser calibration data and MC	21
3.7	Schematic view of the black sheet reflectivity measurement	22
4.1	HKKM11 atmospheric neutrino flux model predictions for the Kamioka site and the measured energy spectra of the atmospheric ν_e and ν_μ fluxes by some experiments	23
4.2	Atmospheric neutrino-antineutrino flux ratio predicted by the HKKM11 model for the Kamioka site	24
4.3	NCQE cross section on nucleon and on oxygen nucleus	24
4.4	Ratio of the BBBA05 form factors to G_d	25
4.5	Ratio of data from the ANNRI experiment by MC with the ANNRI-Gd model for the single gamma-ray events	25
5.1	Schematic view of a cone and its angle defined by a combinations of 3-PMT hits	26

List of Tables

1.1	Three-neutrino mixing parameters and δ_{CP}	6
2.1	Information of each observation phase	13
2.2	Cherenkov threshold of main charged particles	14
2.3	Trigger threshold and time width for recording PMT hits of each trigger type in SK-VI	17

1 Introduction

1.1 Neutrino

Neutrinos, which are Fermions with spin of 1/2, are classified as leptons that do not participate in the strong interaction in the Standard Model (SM) of the particle physics. Moreover, neutrinos do not have charge, and the neutrino mass is so tiny that the gravitational interaction can be ignored. Therefore, neutrinos interact with other particles only via the weak interaction, and are difficult to observe. The name "neutrino" was named by E. Fermi in 1933 [1]. The name comes from the "neutral" that means the zero charge, and "ino" that means small in Italian. Currently, we know that there are three flavors of neutrinos: electron neutrino, muon neutrino, and tau neutrino.

The existence of neutrinos was suggested by W. Pauli in 1930 [1]. Once, the energy spectrum of the electron emitted by the beta decay was expected to be the line spectrum. However, in 1914, J. Chadwick found that the energy spectrum was not the line spectrum but the continuous spectrum [2]. To explain the continuous spectrum of the electron reported by Chadwick, Pauli claimed that an unknown particle with spin of 1/2 and zero charge is emitted in the beta decay in addition to the electron. In 1956, more than 20 years after Pauli proposed the existence of neutrinos, (electron anti)neutrinos produced in nuclear reactors were discovered by F. Reines and C. Cowan [3]. In 1962, muon neutrinos were discovered in the accelerator experiment by L. Lederman, M. Schwartz, and J. Steinberger [4]. In 2001, tau neutrinos were discovered in the DONUT (Direct Observation of NU Tau) experiment [5].

1.2 Neutrino oscillation

In the SM, the neutrino mass is zero [6]. However, in 1998, the evidence for the neutrino oscillation was discovered in the Super-Kamiokande and it was proved that the neutrino mass is not zero [7]. Neutrino oscillation is a phenomenon that the flavor of neutrino changes while the neutrino passes through a space.

Here the neutrino oscillation in vacuum is considered. The flavor eigenstate $|\nu_\alpha\rangle$ is represented by the superposition of the mass eigenstate $|\nu_i\rangle$,

$$|\nu_\alpha\rangle = \sum_{i=1}^n U_{\alpha i}^* |\nu_i\rangle, \quad (1.1)$$

where n ($= 3$) is the number of neutrino species and U is a 3×3 unitary matrix, called the Pontecorvo-Maki-Nakagawa-Sakata (PMNS) mixing matrix. This matrix consists of four independent parameters (three mixing angles, θ_{12} , θ_{23} , and θ_{13} , and one phase angle δ_{CP}),

$$\begin{aligned} U &= \begin{pmatrix} 1 & 0 & 0 \\ 0 & c_{23} & s_{23} \\ 0 & -s_{23} & c_{23} \end{pmatrix} \begin{pmatrix} c_{13} & 0 & s_{13}e^{-i\delta_{\text{CP}}} \\ 0 & 1 & 0 \\ -s_{13}e^{i\delta_{\text{CP}}} & 0 & c_{13} \end{pmatrix} \begin{pmatrix} c_{12} & s_{12} & 0 \\ -s_{12} & c_{12} & 0 \\ 0 & 0 & 1 \end{pmatrix} \\ &= \begin{pmatrix} c_{12}c_{13} & s_{12}c_{13} & s_{13}e^{-i\delta_{\text{CP}}} \\ -s_{12}c_{23} - c_{12}s_{23}s_{13}e^{i\delta_{\text{CP}}} & c_{12}c_{23} - s_{12}s_{23}s_{13}e^{i\delta_{\text{CP}}} & s_{23}c_{13} \\ s_{12}s_{23} - c_{12}c_{23}s_{13}e^{i\delta_{\text{CP}}} & -c_{12}s_{23} - s_{12}c_{23}s_{13}e^{i\delta_{\text{CP}}} & c_{23}c_{13} \end{pmatrix}, \end{aligned} \quad (1.2)$$

where $c_{ij} \equiv \cos \theta_{ij}$ and $s_{ij} \equiv \sin \theta_{ij}$. After traveling a distance L ($\simeq ct$ for relativistic neutrinos), the flavor eigenstate evolves as

$$|\nu_\alpha(t)\rangle = \sum_{i=1}^n U_{\alpha i}^* |\nu_i(t)\rangle, \quad (1.3)$$

where $|\nu_i(t)\rangle = e^{-iE_i t} |\nu_i(0)\rangle$ (E_i is the energy of the neutrino mass eigenstate ν_i). At that time, the probability of being observed as the flavor eigenstate $|\nu_\beta\rangle$ is

$$P_{\alpha\beta} = |\langle\nu_\beta|\nu_\alpha(t)\rangle|^2 = \left| \sum_{i=1}^n \sum_{j=1}^n U_{\alpha i}^* U_{\beta j} \langle\nu_j|\nu_i(t)\rangle \right|^2. \quad (1.4)$$

Here, neutrinos are relativistic, thus $p_i \simeq p_j \equiv p \simeq E$. Therefore, E_i can be approximated as

$$E_i = \sqrt{p_i^2 + m_i^2} = p_i \sqrt{1 + \frac{m_i^2}{p_i^2}} \simeq p_i \left(1 + \frac{m_i^2}{2p_i^2}\right) \simeq E + \frac{m_i^2}{2E}. \quad (1.5)$$

Using Equation (1.5) and the orthogonality of the mass eigenstates, $\langle\nu_j|\nu_i\rangle = \delta_{ij}$, Equation (1.4) can be expressed as

$$P_{\alpha\beta} = \delta_{\alpha\beta} - 4 \sum_{i < j}^n \text{Re}[U_{\alpha i} U_{\beta i}^* U_{\alpha j}^* U_{\beta j}] \sin^2 X_{ij} + 2 \sum_{i < j}^n \text{Im}[U_{\alpha i} U_{\beta i}^* U_{\alpha j}^* U_{\beta j}] \sin 2X_{ij}, \quad (1.6)$$

where

$$X_{ij} = \frac{(m_i^2 - m_j^2)L}{4E} \equiv \frac{\Delta m_{ij}^2 L}{4E} = 1.267 \frac{\Delta m_{ij}^2}{\text{eV}^2} \frac{L/E}{\text{m/MeV}}. \quad (1.7)$$

The neutrino oscillation between two neutrino species in vacuum is described in Appendix A. Moreover, the neutrino oscillation in matter is described in Ref. [8].

From the above calculation, it can be seen that the neutrino oscillation can be described by six parameters (θ_{12} , θ_{23} , θ_{13} , Δm_{21}^2 , Δm_{32}^2 , and δ_{CP}). These parameters can be measured by observing the oscillation phenomena of solar neutrinos, atmospheric neutrinos, reactor neutrinos, and accelerator neutrinos. Table 1.1 shows the three-neutrino mixing parameters and δ_{CP} . Currently, the values of m_1 , m_2 , and m_3 and the magnitude relationship between m_2 and m_3 are not yet known. There are two possibilities of the neutrino mass ordering: Normal Ordering (NO, $m_1 < m_2 < m_3$) or Inverted Ordering (IO, $m_3 < m_1 < m_2$).

1.3 Supernova explosion

1.4 Current status of DSNB search

1.5 Neutrino-oxygen NCQE reactions

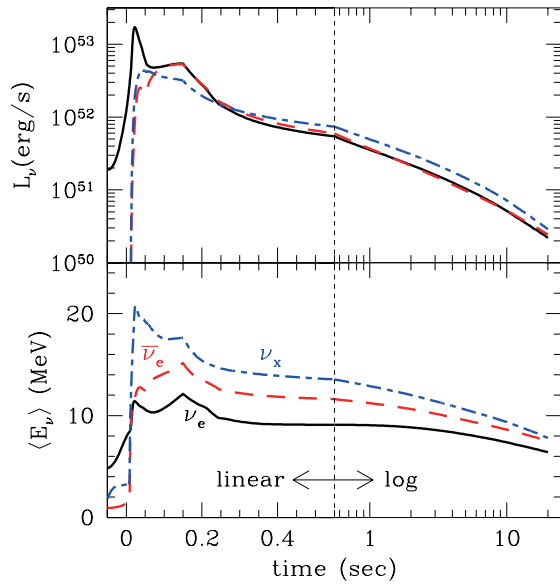


Figure 1.1: Time evolution of the luminosity and average energy of neutrinos [10].

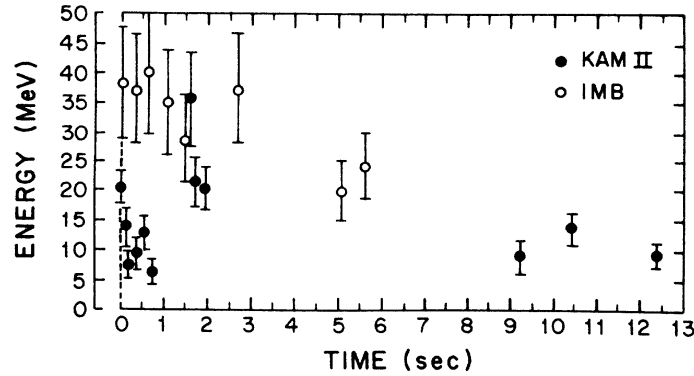


Figure 1.2: Events from SN1987A observed in Kamiokande-II and the IMB detector [11].

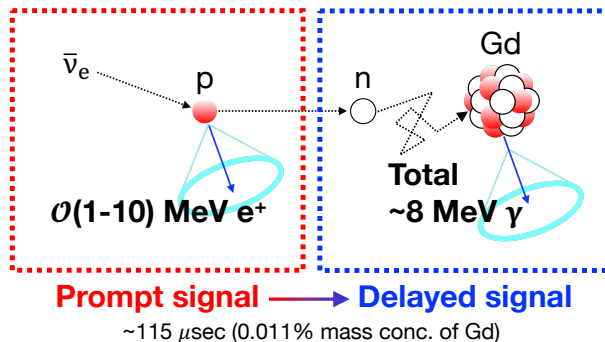


Figure 1.3: Schematic view of the DSNB event.

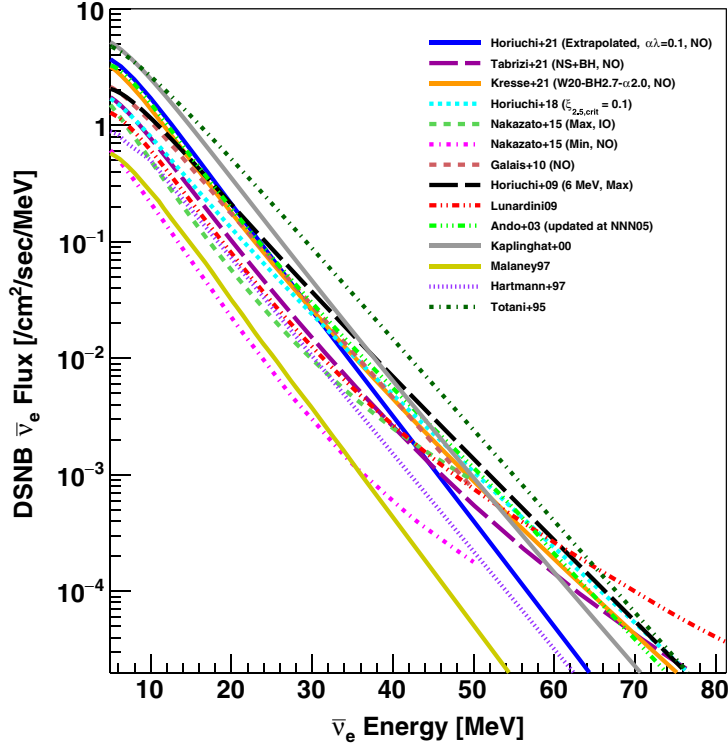


Figure 1.4: Predictions of DSNB $\bar{\nu}_e$ flux from various theoretical models [12].

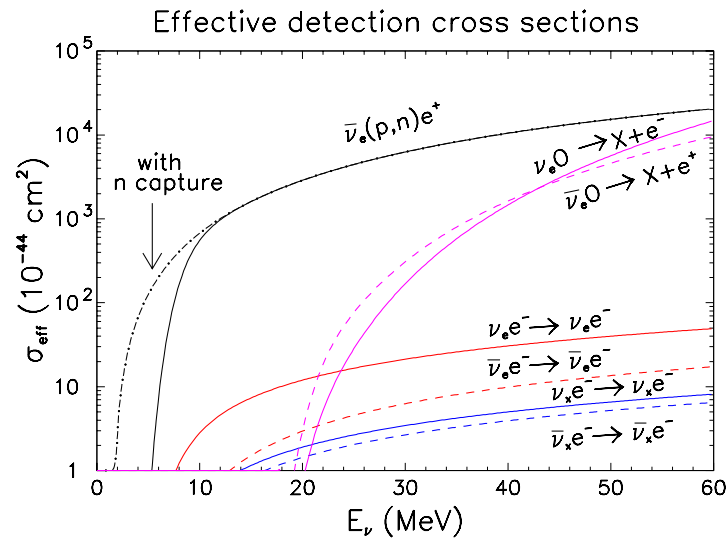


Figure 1.5: Effective neutrino interaction cross sections including energy resolution and threshold effects in large water Cherenkov detectors [13]. Horizontal axis shows the neutrino energy.

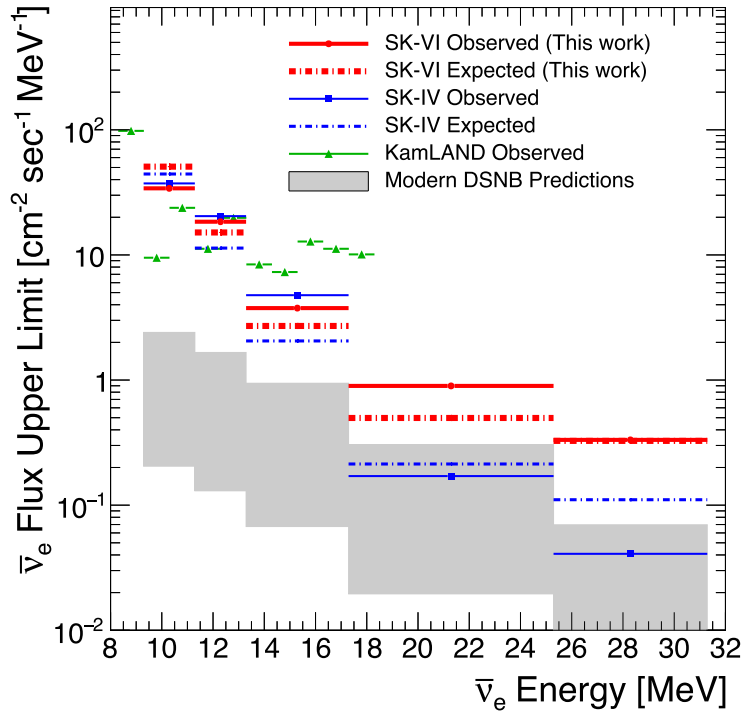


Figure 1.6: Upper limit of the $\bar{\nu}_e$ flux in the SK-Gd DSNB search [14].

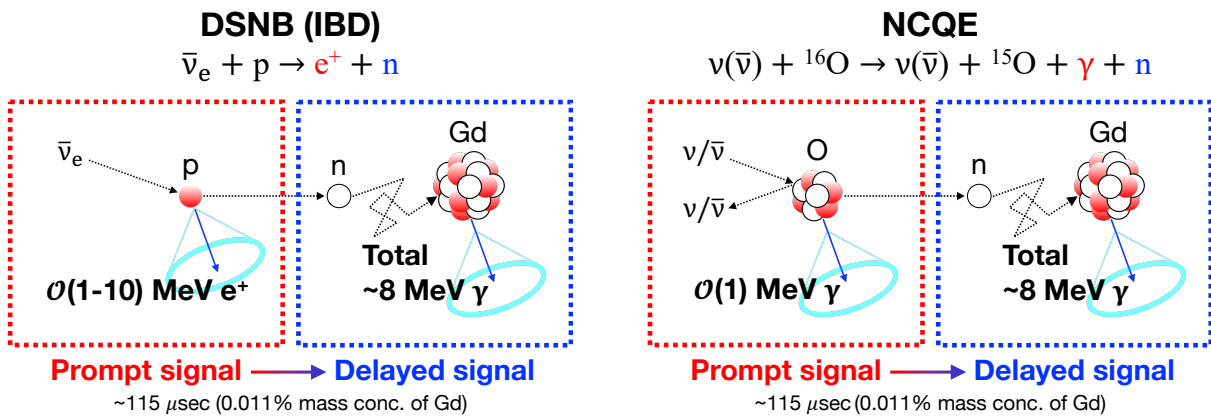


Figure 1.7: Schematic view of the DSNB and NCQE events.

Table 1.1: Three-neutrino mixing parameters and δ_{CP} [9]. Here, $\theta_{ij} \in [0, \pi/2]$ and $\delta_{\text{CP}} \in [0, 2\pi]$.

$\sin^2 \theta_{12}$	0.307 ± 0.013
$\sin^2 \theta_{23}$ (NO)	$0.547^{+0.018}_{-0.024}$
$\sin^2 \theta_{23}$ (IO)	$0.534^{+0.021}_{-0.024}$
$\sin^2 \theta_{13}$	$(2.20 \pm 0.07) \times 10^{-2}$
Δm_{21}^2	$(7.53 \pm 0.18) \times 10^{-5} \text{ eV}^2$
Δm_{32}^2 (NO)	$(2.437 \pm 0.033) \times 10^{-3} \text{ eV}^2$
Δm_{32}^2 (IO)	$(-2.519 \pm 0.033) \times 10^{-3} \text{ eV}^2$
δ_{CP}	$1.23 \pm 0.21 \pi \text{ rad}$

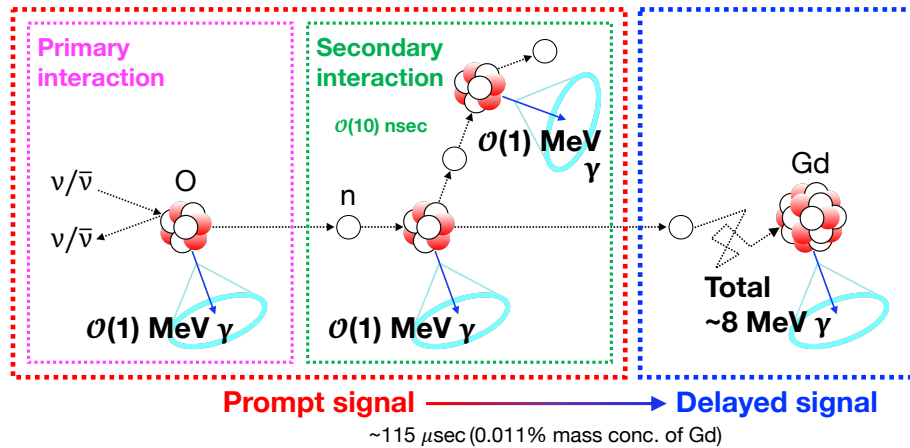


Figure 1.8: Schematic view of the NCQE event. Prompt signal consists of de-excitation gamma-rays from atmospheric neutrino-oxygen nucleus interaction (primary interaction) and nucleon-oxygen nucleus interaction (secondary interaction).

2 Super-Kamiokande

2.1 Super-Kamiokande

The Super-Kamiokande (SK) [15] is the experiment held in Kamioka, Gifu, Japan, with the large water Cherenkov detector placed in 1,000 m underground, 2,700 m water equivalent overburden. The overview of the SK detector is shown in Figure 2.1. The SK stands for “Super-Kamioka Neutrino Detection Experiment” and “Super-Kamioka Nucleon Decay Experiment”. The rate of cosmic ray muon is reduced by a factor of 10^5 compared to that of the ground level.

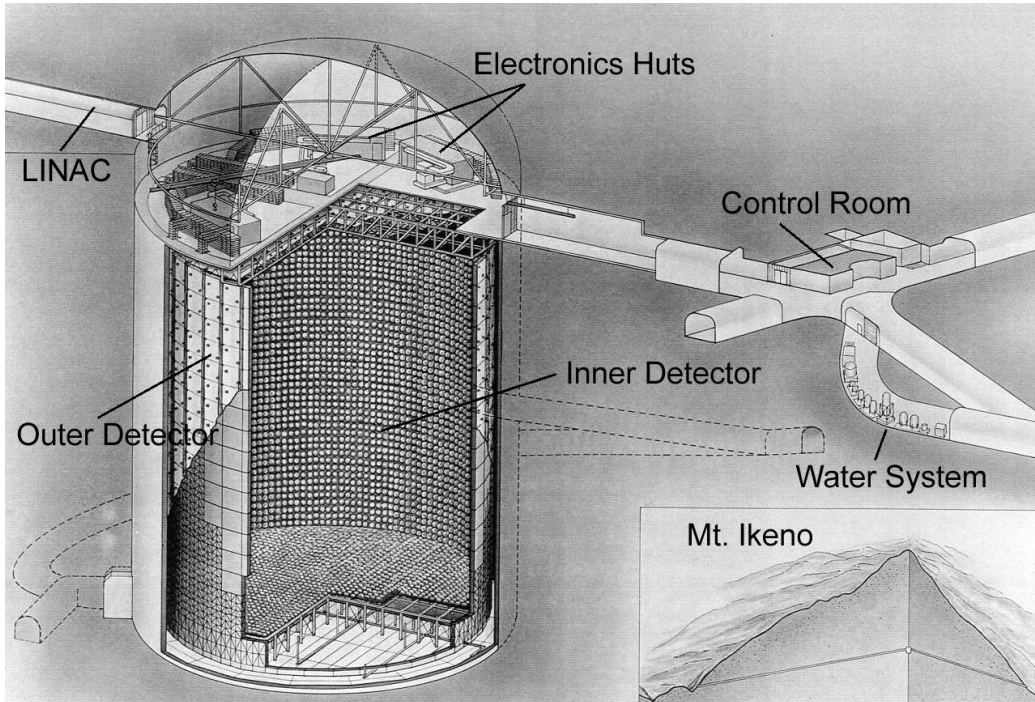


Figure 2.1: Overview of the SK detector [15].

The SK detector consists of the stainless-steel cylindrical tank with a diameter of 39.3 m and a height of 41.4 m and 50 kilotons ultrapure water. The tank is separated into the inner detector (ID) and the outer detector (OD) by stainless-steel frames (supermodule frames). The cross section of the SK detector and the overview of supermodule frames are shown in Figure 2.2. The diameter of ID, the height of ID and the volume of ID (the fiducial volume) is 33.8 m, 36.2 m and 32 kilotons (22.5 kilotons), respectively. In ID, 11,129 20-inch (50 cm) photomultiplier tubes (PMTs) are installed. The gaps between ID PMTs are covered by black polyethylene terephthalate sheets. The sheets separate ID and OD optically and suppress the reflection at the surface of the ID wall. Moreover, the sheets reduce low energy events by radioactive backgrounds occurring behind the PMTs. On the other hand, in OD, 1,885 8-inch (20 cm) PMTs are installed. OD volume is covered by white Tyvek sheets manufactured by DuPont. The Tyvek sheets have high reflectivity and enhance the light collection efficiency in OD.

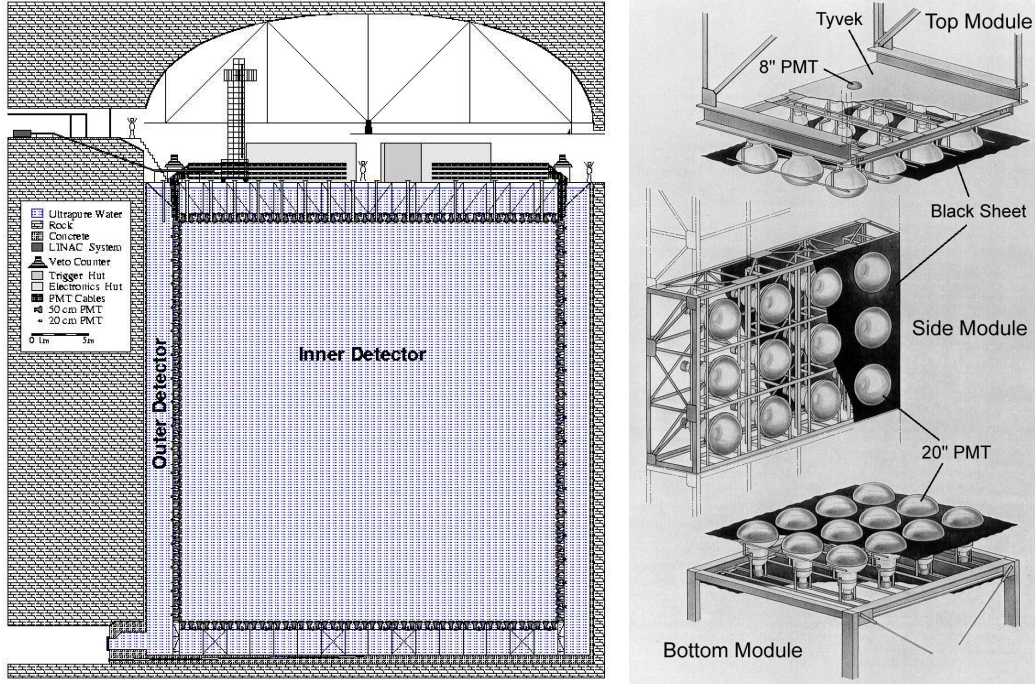


Figure 2.2: Cross section of the SK detector (left) and overview of supermodule frames (right) [15].

2.2 ID PMT and OD PMT

The schematic view of the ID PMT is shown in Figure 2.3. The number of ID PMTs is 7,650 on the barrel (side walls), 1,740 on the top and 1,739 on the bottom, and the effective photocathode coverage of ID is 40%. The role of ID PMTs is to reconstruct the energy, generated position, direction and the kind of the charged particles. Figure 2.4 shows the quantum efficiency of the ID PMT photocathode as a function of wavelength. The material of photocathode is bialkali (Sb-K-Cs) and the quantum efficiency is about 21% at 360 - 400 nm. Figure 2.5 shows the single photoelectron pulse height distribution of the ID PMT. The peak around zero ADC count is caused by PMT dark current. Figure 2.6 shows the relative transit time distribution for a typical ID PMT tested using 410 nm wavelength light at the single photoelectron intensity level. The 1σ of transit time for a single photoelectron signal is 2.16 ns.

The number of OD PMTs is 1,275 on the barrel, 302 on the top and 308 on the bottom. To compensate the small number of OD PMTs, wavelength shifting (WS) plate is attached to each OD PMT. The WS plate is square acrylic panel with a side of 60 cm and a thickness of 1.3 cm, doped with 50 mg/L of bis-MSB ($C_{24}H_{22}$). The WS plate absorbs UV light, and then emit photons in the blue - green. OD PMT with bialkali photocathode is more sensitive to blue - green photons than UV photons. Therefore, the light collection efficiency is improved by about a factor of 1.5 compared to without WS plates. The timing resolution of OD PMTs with WS plates is 15 ns (FWHM), which is poorer than that of ID PMTs. However, OD was optimized as a veto counter and the poorer timing resolution is less important. Figure 2.7 shows the positional relationship of ID PMTs and OD PMTs in a supermodule frame. Basically, in a supermodule frame, 12 ID PMTs and 2 OD PMTs are attached.

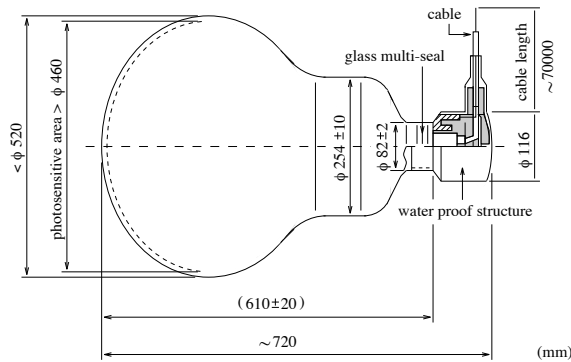


Figure 2.3: Schematic view of the ID PMT [15].

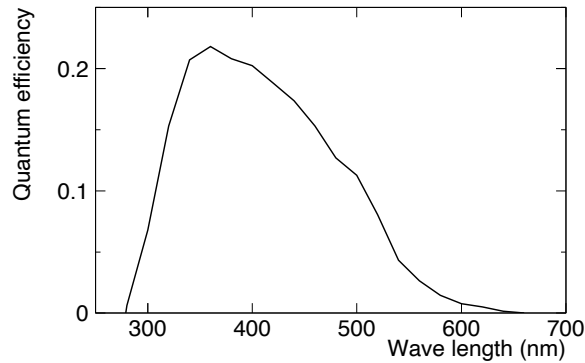


Figure 2.4: Quantum efficiency of the ID PMT photocathode as a function of wavelength [15]. The material of ID PMT photocathode is bialkali (Sb-K-Cs).

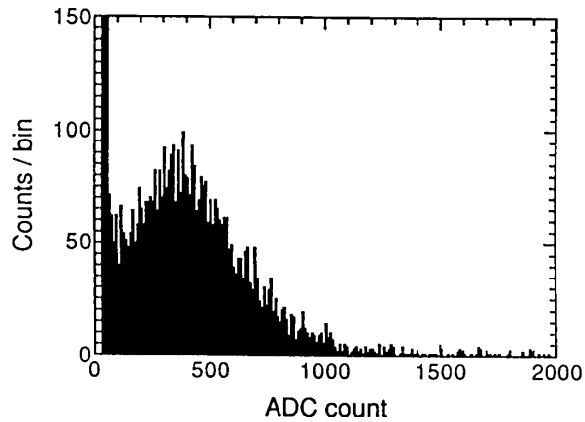


Figure 2.5: Single photoelectron pulse height distribution of the ID PMT [15]. The peak around zero ADC count is caused by PMT dark current.

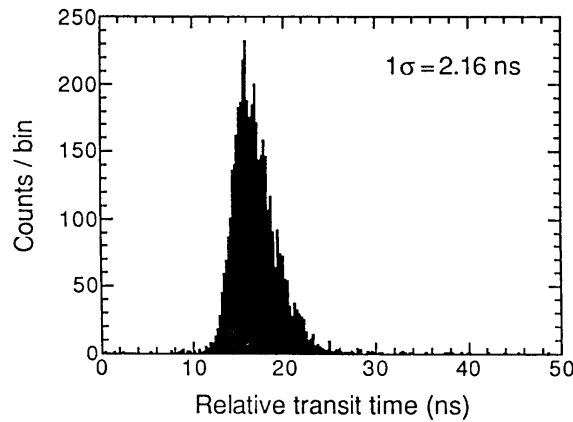


Figure 2.6: Relative transit time distribution for a typical ID PMT tested using 410 nm wavelength light at the single photoelectron intensity level [15].

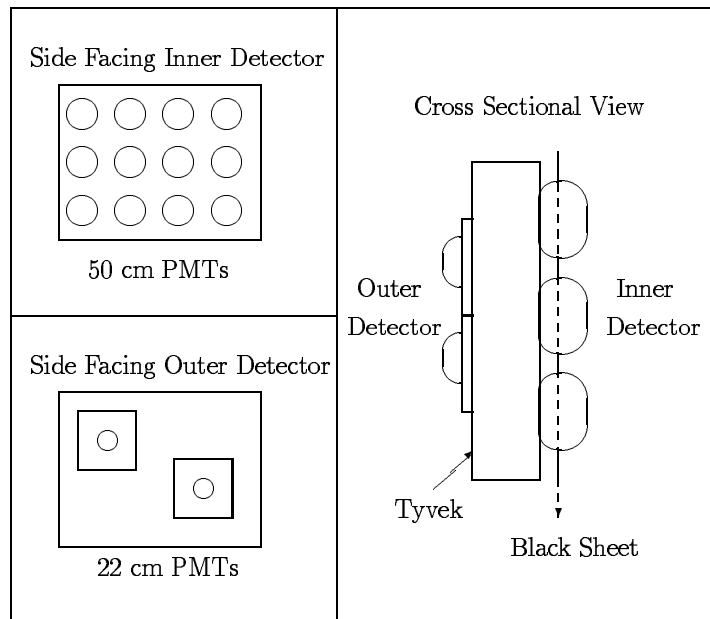


Figure 2.7: Positional relationship of ID PMTs and OD PMTs in a supermodule frame [16]. 12 ID PMTs and 2 OD PMTs are attached in a supermodule frame, basically.

2.3 Helmholtz coils

The geomagnetic field would affect photoelectron trajectories and timing in the PMTs. Therefore, 26 sets of horizontal and vertical Helmholtz coils are deployed around the inner surface of the tank to reduce the geomagnetic field. Figure 2.8 shows the schematic view of Helmholtz coils. The average geomagnetic field intensity without Helmholtz coils is about 450 mG [15]. The average field intensity can be reduced to 32 mG with Helmholtz coils, resulting that the deviation in the collection efficiency of photoelectrons is 2% [17].

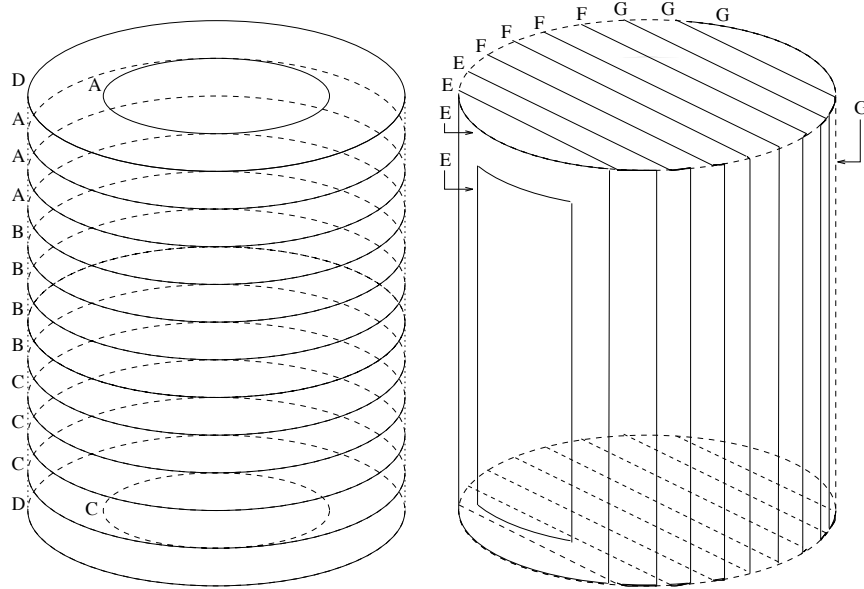


Figure 2.8: Schematic view of Helmholtz coils [18].

2.4 Observation phase

The observation phase of SK is categorized into seven, from SK-I to SK-VII. Each observation phase is described below.

SK-I

SK-I started in April 1996 and ended in July 2001. In ID, 11,146 PMTs were attached and the effective photocathode coverage of ID was 40%. It was during the SK-I that we got the evidence for neutrino oscillation [7].

SK-II

In November 12th, 2001, one bottom PMT broke when ultrapure water was filled into SK detector after finishing the detector maintenance. Due to the shockwave generated at that time, other PMTs were broken in a chain. As a result, it became a serious accident that 6,779 ID PMTs and 1,017 OD PMTs were lost. In SK-II, which started in October 2002 and ended in October 2005, the observation was performed using 5,182 remained and spare ID PMTs and 1,885 remained and new OD PMTs. The effective photocathode



Figure 2.9: Picture of a shockwave prevention case [19].

coverage of ID was 19%. Since SK-II, each ID PMT has been covered with a shockwave prevention case. The case consists of an acrylic that covers the photocathode and Fiber Reinforced Plastic (FRP) case that covers parts other than the photocathode. The case not only prevents shockwave but also increases the water pressure resistance of the PMT. The picture of a shockwave prevention case is shown in Figure 2.9.

SK-III

SK-III started in July 2006 and ended in August 2008. Since SK-III, the number of ID PMTs has been 11,129 and the effective photocathode coverage of ID has been 40%. The reason why the number of ID PMTs is reduced by 17 compared to SK-I is that ID PMTs cannot be installed at the edge of the detector because the size of the shockwave prevention case is large.

SK-IV

In September 2008, the data acquisition system was renewed from Analog Timing Module (ATM) to QTC-Based Electronics with Ethernet (QBEE) and SK-IV started [20]. QTC stands for charge-to-time converter. The renewal of the system allows us to open the data acquisition time window until $535\ \mu\text{s}$ from the trigger timing and enabled to search neutron signals [21]. SK-IV continued until June 2018 and is longest phase at this time.

SK-V

The tank refurbishment work toward the SK-Gd experiment was conducted between SK-IV and SK-V. The purpose of the work was the water stop reinforcement of the tank, the piping improvement in the tank and the PMT replacement. After finishing the work, SK-V started in January 2019 and ended in July 2020.

SK-VI

In July 2020, we dissolved 13.2 tons of $\text{Gd}_2(\text{SO}_4)_3 \cdot 8\text{H}_2\text{O}$ (we introduced 0.011% of Gd) into the SK tank and SK-VI (the SK-Gd experiment) started. The time constant of neutron capture at this Gd concentration is about $115\ \mu\text{s}$ [22]. SK-VI continued until June 2022.

SK-VII

In June 2022, we additionally dissolved 27.3 tons of $\text{Gd}_2(\text{SO}_4)_3 \cdot 8\text{H}_2\text{O}$ into the SK tank and SK-VII

started. The Gd concentration is comparable to 0.03%. The time constant of neutron capture at this Gd concentration is about $62\ \mu\text{s}$.

The information of each observation phase is summarized in Table 2.1.

Table 2.1: Information of each observation phase.

Phase	SK-I	SK-II	SK-III
Start	Apr. 1996	Oct. 2002	Jul. 2006
End	Jul. 2001	Oct. 2005	Sep. 2008
# of ID PMTs (Coverage)	11,146 (40%)	5,182 (19%)	11,129 (40%)
# of OD PMTs	1,885	1,885	1,885
Electronics	ATM	ATM	ATM
Gd concentration	0%	0%	0%

Phase	SK-IV	SK-V	SK-VI	SK-VII
Start	Sep. 2008	Jan. 2019	Jul. 2020	Jun. 2022
End	Jun. 2018	Jul. 2020	Jun. 2022	-
# of ID PMTs (Coverage)	11,129 (40%)	11,129 (40%)	11,129 (40%)	11,129 (40%)
# of OD PMTs	1,885	1,885	1,885	1,885
Electronics	QBEE	QBEE	QBEE	QBEE
Gd concentration	0%	0%	0.011%	0.03%

2.5 Detection principle

When the speed of the charged particle passing through the dielectric medium is faster than the speed of light in the medium, photons are radiated conically along the track of the particle. This phenomenon is called “Cherenkov radiation”, and the radiated photons are called “Cherenkov photons”. Figure 2.10 shows the schematic view of Cherenkov radiation. The Cherenkov photons are projected in a ring as shown in left side of Figure 2.10. The ring is called “Cherenkov ring”. In the SK, the energy, generated position, direction and the kind of the charged particle are reconstructed using the time, quantity of charge and Cherenkov ring pattern information that ID PMTs received. In right side of Figure 2.10, the charged particle with velocity v moves distance $vt = \frac{v}{c}ct = \beta ct$ in time t , where c is the speed of light in vacuum and $\beta = \frac{v}{c}$ is the ratio of v and c . While the Cherenkov photon moves distance $\frac{c}{n}t$ in time t , where n is the refractive index of the dielectric medium. Therefore, when the angle between the direction of charged particle and the direction of Cherenkov photon is defined as θ_C , the next formula is established,

$$\cos \theta_C = \frac{\frac{c}{n}t}{\beta ct} = \frac{1}{n\beta}. \quad (2.1)$$

In Equation (2.1), assuming that $n = 1.34$, which is the refractive index of water, and $\beta = 1$, θ_C becomes about 42° . Therefore, in water, the maximum angle between the direction of charged particle and the direction of Cherenkov angle is about 42° .

The energy E required for the charged particle with rest mass m to emit Cherenkov photons (Cherenkov

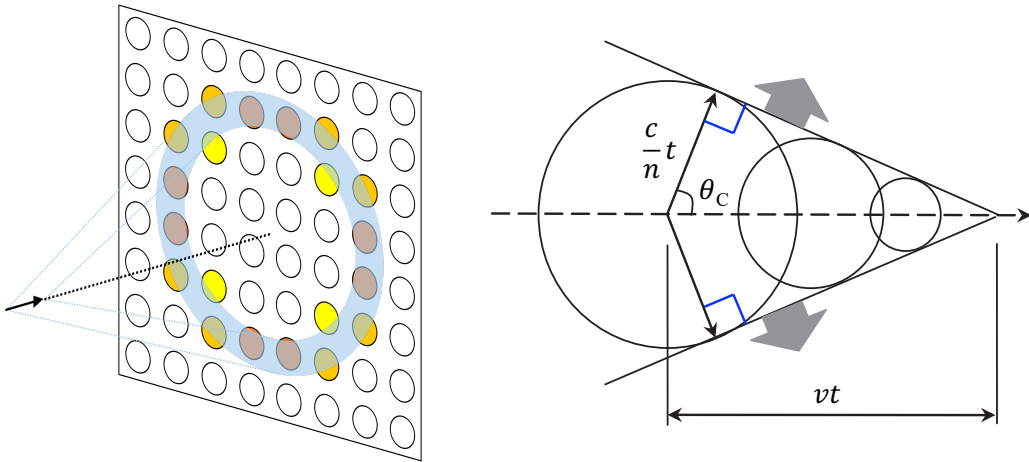


Figure 2.10: Schematic view of Cherenkov radiation [23].

threshold) is

$$E = \frac{mc^2}{\sqrt{1 - \beta^2}} \geq \frac{mc^2}{\sqrt{1 - \left(\frac{1}{n}\right)^2}} = \frac{nmc^2}{\sqrt{n^2 - 1}}. \quad (2.2)$$

The Cherenkov threshold of main charged particles is summarized in Table 2.2.

Assuming that the wavelength region of Cherenkov photons is from λ_1 to λ_2 , the number of Cherenkov photons N emitted per unit length x when the particle with charge z passes through the medium is

$$\frac{dN}{dx} = 2\pi\alpha z^2 \sin^2 \theta_C \left(\frac{1}{\lambda_1} - \frac{1}{\lambda_2} \right), \quad (2.3)$$

where α is the fine-structure constant.

Table 2.2: Cherenkov threshold of main charged particles [6]. m is rest mass and E is Cherenkov threshold. Here $n = 1.34$ is assumed.

Charged particle	e^\pm	μ^\pm	π^\pm	K^\pm	p
m [MeV/ c^2]	0.511	105.658	139.570	493.677	938.272
E [MeV]	0.768	158.730	209.676	741.652	1,409.568

2.6 Water purification system

The 50 kilotons ultrapure water of the SK is made from the groundwater of the Kamioka mine. The groundwater contains the dust, bacteria and radioactive impurities. These impurities should be removed to avoid decreasing the water transparency and increasing low energy backgrounds. In the SK, these impurities are removed by circulating and purifying the ultrapure water using the water purification system at a flow rate of 120 m³/h. Figure 2.11 shows the schematic view of water purification system. This system consists of three systems: the dissolving system, the pretreatment system and the re-circulation system. The dissolving system and the pretreatment system are used during Gd loading, while the re-circulation system is used during both Gd loading and data taking. Here each component of re-circulation system is described below.

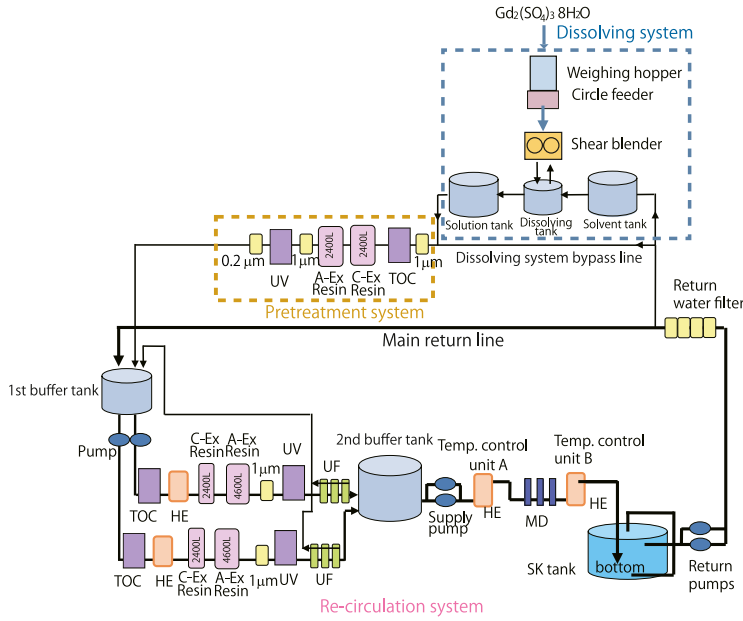


Figure 2.11: Schematic view of water purification system [22]. The dissolving system and the pretreatment system are used during Gd loading, while the re-circulation system is used during both Gd loading and data taking.

- UV total organic carbon reduction lamp (TOC): TOC lamp oxidatively decomposes carbon and other compounds. These are eventually decomposed into water and carbon dioxide.
- Heat exchanger (HE): High water temperature causes the bacterial growth, the decrease of water transparency and the increase of PMT dark noise. HE keeps the water temperature around 13 °C at a precision better than 0.01 °C.
- Strongly acidic cation exchange resin (C-Ex Resin): C-Ex Resin removes positively charged impurities, and radium ions in particular, while preserving the dissolved gadolinium ions (Gd^{3+}).
- Strongly basic anion exchange resin (A-Ex Resin): A-Ex Resin removes negatively charged impurities while preserving the dissolved sulfate ions (SO_4^{2-}).
- One micron filter (1 μm): 1 μm filter removes the dusts larger than 1 μm.
- UV sterilizer (UV): UV sterilizer kills the bacteria.
- Ultrafiltration modules (UF): UF modules remove tiny dusts.
- Membrane degasifier (MD): MD removes radon dissolved in the ultrapure water.

2.7 Air purification system

Most of radioactive backgrounds come from radon, which is rich in the rock of the Kamioka mine. To reduce radioactive backgrounds, radon in the air should be reduced as much as possible.

Figure 2.12 shows the typical radon concentration in the air at the SK over a year. Radon concentration in

the air of the mine is 2,000 - 3,000 Bq/m³ during the warm season, from May to October, while the concentration is 100 - 300 Bq/m³ in the cold season, from November to April. This is because the airflow inside the mine changes depending on the temperature outside the mine. To keep the concentration below 100 Bq/m³ inside the experimental area, fresh air is continuously blown at a flow rate of 10 m³/min from outside the mine (Radon Hut) to the experimental area through an air duct. The flow rate makes the air pressure inside the experimental area higher than outside, minimizing the entry of the air outside the experimental area. As a result, the concentration inside the experimental area is kept at 30 - 50 Bq/m³ throughout the year, as shown in Figure 2.12.

However, the radon concentration inside the experimental area is still too high for observations with low radioactive backgrounds. Therefore, the fresh air is purified using the air purification system, then the purified air is supplied to the gap between the top of the SK tank and the water surface. Figure 2.13 shows the schematic view of air purification system. Each component of air purification system is described in Ref. [24]. The residual radon concentration in the purified air is a few mBq/m³.

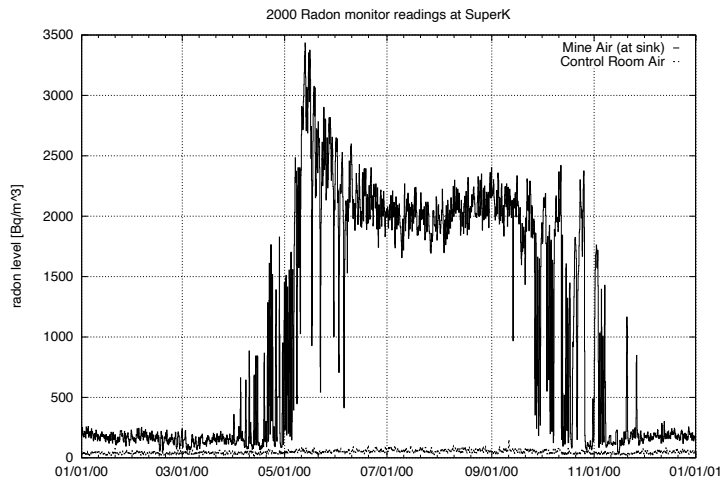


Figure 2.12: Typical radon concentration in the air at the SK over a year [15]. The solid line shows the concentration outside the experimental area. The dashed line shows the concentration inside the experimental area.

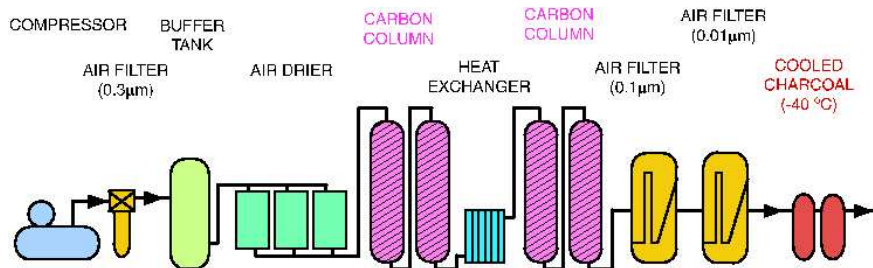


Figure 2.13: Schematic view of air purification system [15]. Each component of air purification system is described in Ref. [24].

2.8 Data acquisition system

As explained in Sec. 2.4, the data acquisition system was changed from ATM to QBEE in SK-IV. The data used in this thesis was acquired by QBEE. Therefore, the description of ATM is omitted in this thesis.

Figure 2.14 shows the schematic view of the data acquisition system after SK-IV. One QBEE board has 8 QTCs, and one QTC has 3 analog input channels for PMT signals. That is, one QBEE board has 24 analog input channels for PMT signals. Figure 2.15 shows the block diagram of the QTC and its surroundings. Each analog input channel has three gain ranges: small, medium, and large. The gain ratio of small, medium, and large is set to 1, 1/7, and 1/49, respectively. Also, the charge dynamic range of small, medium, and large is 0.2 - 51 pC, 1 - 357 pC, and 5 - 2500 pC, respectively. The gain ratio is optimized to cover a wide charge dynamic range with reasonable resolution. When the charge is sent to a QBEE board, the QTC integrates the charge and generates the output signal with the width proportional to the integrated charge. Then the output signal is digitized by time-to-digital converter (TDC). The digitized signals are transferred to 20 front-end PCs, and sent to 10 merger PCs. In the merger PCs, the signals from all the front-end PCs are merged and the software trigger is applied. Details about the software trigger is described later. From the merger PCs, signals for triggered events are sent to an organizer PC and then written onto the disk for offline analysis. Details about the front-end PCs, merger in the merger PCs, the organizer PC, and the disk are described in Ref. [25].

The software trigger process scans the signals sent to the merger PCs and searches the events satisfying the trigger conditions. A trigger is applied when the number of ID PMT hits within 200 ns, which corresponds to the time that a Cherenkov photon moves from the edge of the SK tank to other, is a certain value or more. Table 2.3 shows the trigger threshold and time width for recording PMT hits of each trigger type in SK-VI. There are four trigger types for ID: Super Low Energy (SLE), Low Energy (LE), High Energy (HE), and Super High Energy (SHE). Also, OD trigger is applied when the number of OD PMT hits within 200 ns is 22 or more. Basically, when a trigger is applied, all hits from $-5 \mu\text{s}$ to $35 \mu\text{s}$ are recorded, where the trigger timing is $0 \mu\text{s}$. However, in the case of SLE, all hits from $-0.5 \mu\text{s}$ to $1.0 \mu\text{s}$ are recorded due to the high trigger rate.

From SK-IV, a special trigger, AFT, was installed to search delayed neutron capture signals. Previously, AFT trigger was applied when SHE trigger was applied and OD trigger was not applied to avoid the events by cosmic ray muons. However, from SK-V, the condition about OD trigger was removed to study the spallation events by cosmic ray muons. When AFT trigger is applied, all hits from $35 \mu\text{s}$ to $535 \mu\text{s}$ in addition to from $-5 \mu\text{s}$ to $35 \mu\text{s}$ are recorded.

Table 2.3: Trigger threshold and time width for recording PMT hits of each trigger type in SK-VI. $N_{200,\text{ID}}$ and $N_{200,\text{OD}}$ shows the number of ID or OD PMT hits within 200 ns.

Trigger type	Trigger threshold	Time width [μs]
SLE	$N_{200,\text{ID}} \geq 34$	1.5
LE	$N_{200,\text{ID}} \geq 49$	40
HE	$N_{200,\text{ID}} \geq 52$	40
SHE	$N_{200,\text{ID}} \geq 60$	40
OD	$N_{200,\text{OD}} \geq 22$	40

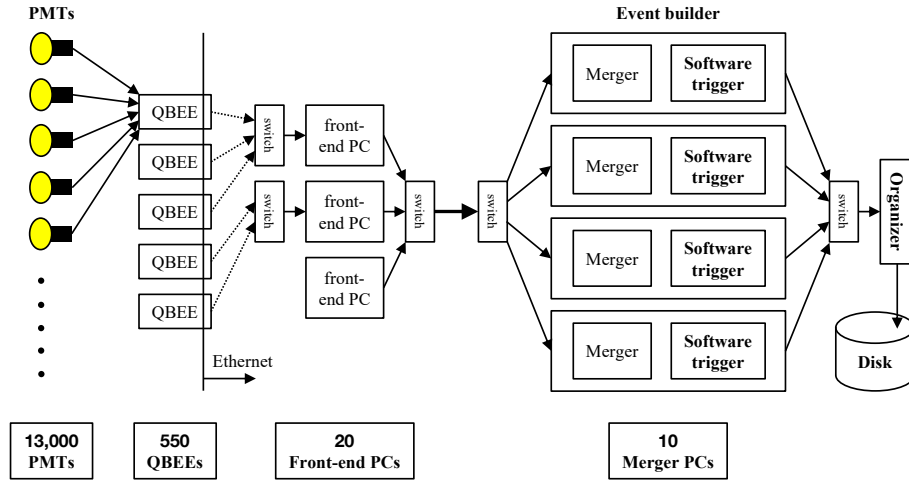


Figure 2.14: Schematic view of the data acquisition system [25].

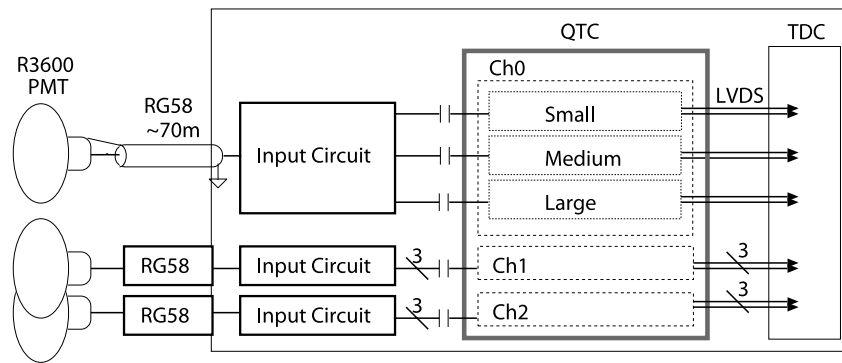


Figure 2.15: Block diagram of the QTC and its surroundings [20]. The output signal of each range (small, medium, or large) is generated by low voltage differential signaling (LVDS) drivers and digitized by time-to-digital converter (TDC).

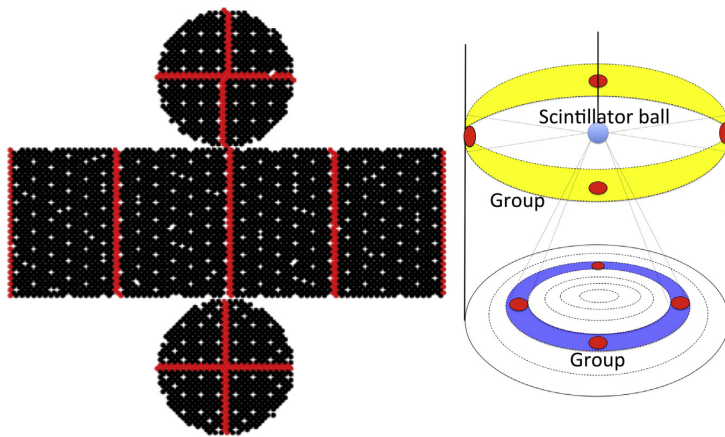


Figure 3.1: Location of standard PMTs in ID (left) and schematic view of the groups of PMTs (right) [17].



Figure 3.2: Picture of the Ni-Cf source.

3 Calibration

3.1 ID detector calibration

ID detector calibration!

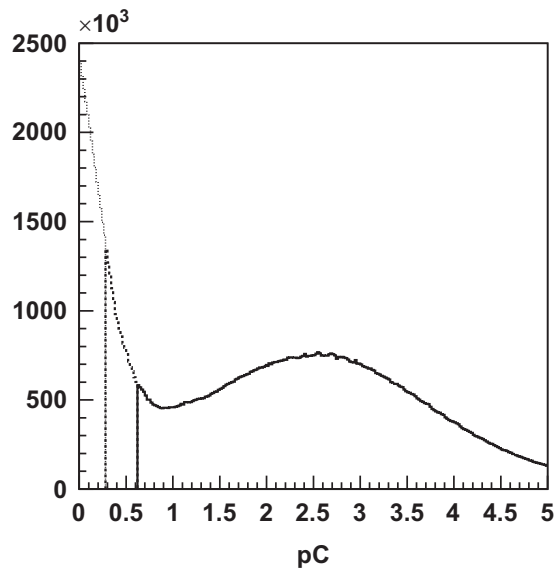


Figure 3.3: Single-pe distribution of the Ni-Cf source data in SK-III [17]. The dashed line shows the data with double gain and half threshold. The dotted line is linear extrapolation.

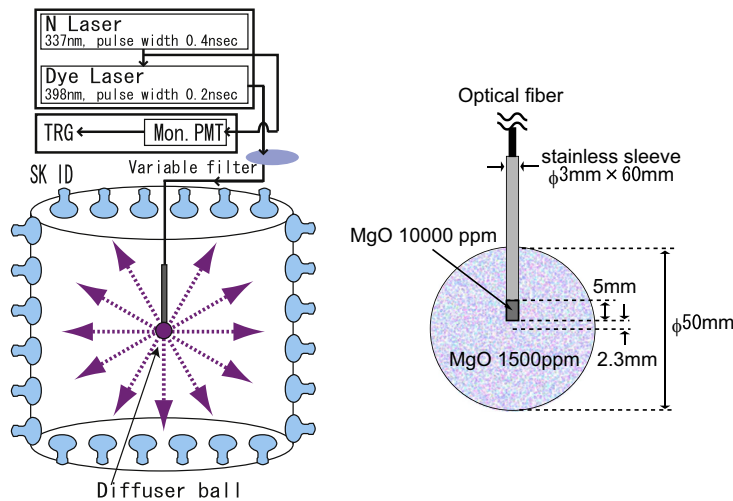


Figure 3.4: Schematic view of the timing calibration system (left) and cross section of the diffuser ball (right) [17].

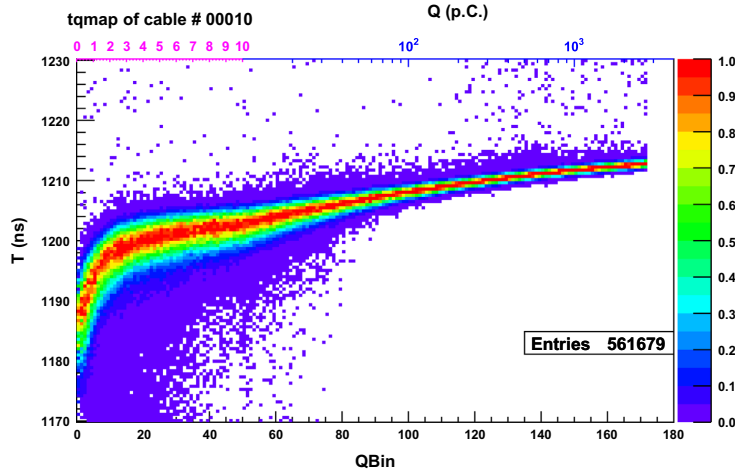


Figure 3.5: Timing and charge distribution for a readout channel [17]. Horizontal axis shows charge (QBin) of each hit. Vertical axis shows TOF-corrected hit timing.

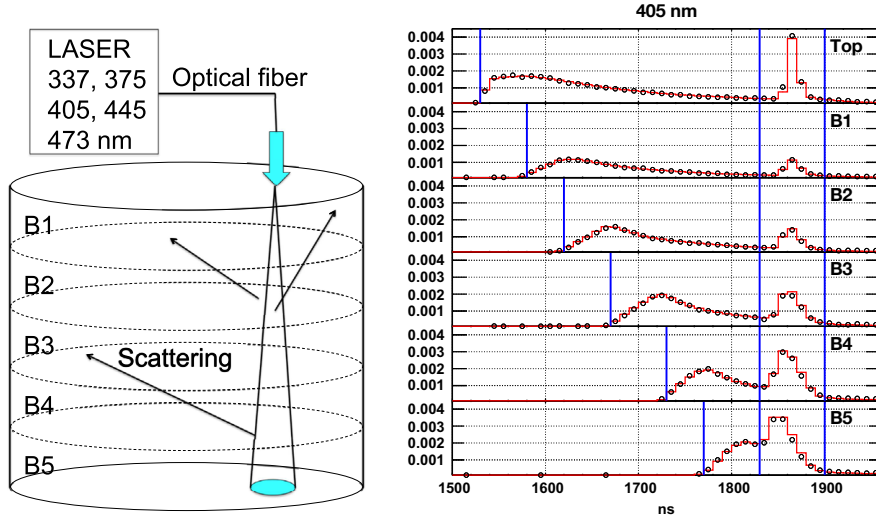


Figure 3.6: Schematic view of the laser calibration system (left) and TOF-subtracted timing distributions of the laser calibration data and MC [17]. Water parameter tuning is performed using top PMTs that are 2 m away from the laser light injector, and barrel PMTs. Barrel is separated into five regions, from B1 to B5. B3 includes PMTs for 11 lines and the others include PMTs for 10 lines. In the left figure, the cyan shaded circle spot on the bottom shows the beam target used in the TOF calculation. In the right figure, the black circle shows data and the red histogram shows MC. Both data and MC are normalized by observed total photoelectrons. Time region between the left two blue solid vertical lines is used for the water parameter tuning. Right time region is used for the PMT reflectivity measurement.

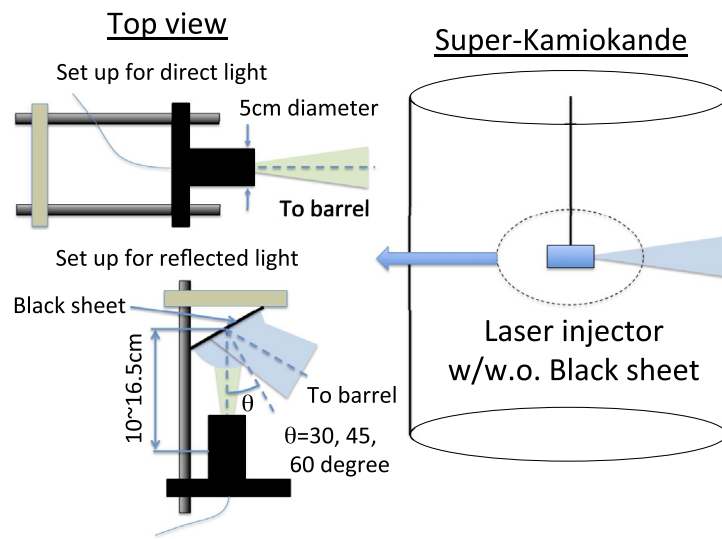


Figure 3.7: Schematic view of the black sheet reflectivity measurement [17]. Left figure shows the top view. The laser light injector is inserted from the top center of the SK tank and the reflected light is measured by ID PMTs.

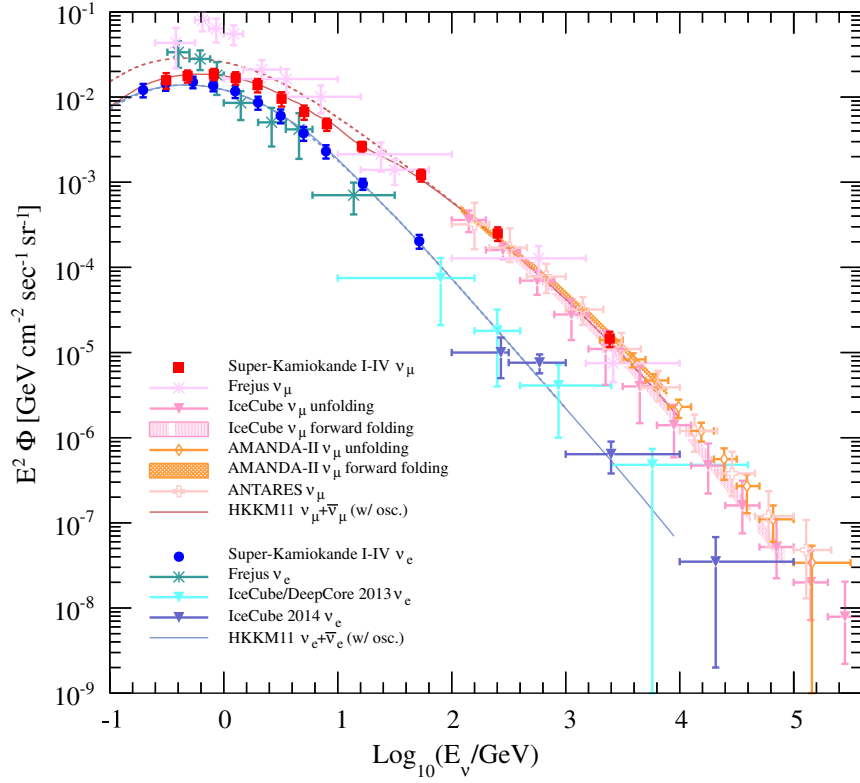


Figure 4.1: HKKM11 atmospheric neutrino flux model predictions for the Kamioka site and the measured energy spectra of the atmospheric ν_e and ν_μ fluxes by some experiments [26, 27].

4 Simulation

4.1 Atmospheric neutrino flux

Atmospheric neutrino flux!

4.2 Neutrino interaction

Neutrino interaction!

4.3 Simulation for the IBD-like event

Simulation for the IBD-like event!

4.4 Detector simulation

Detector simulation!

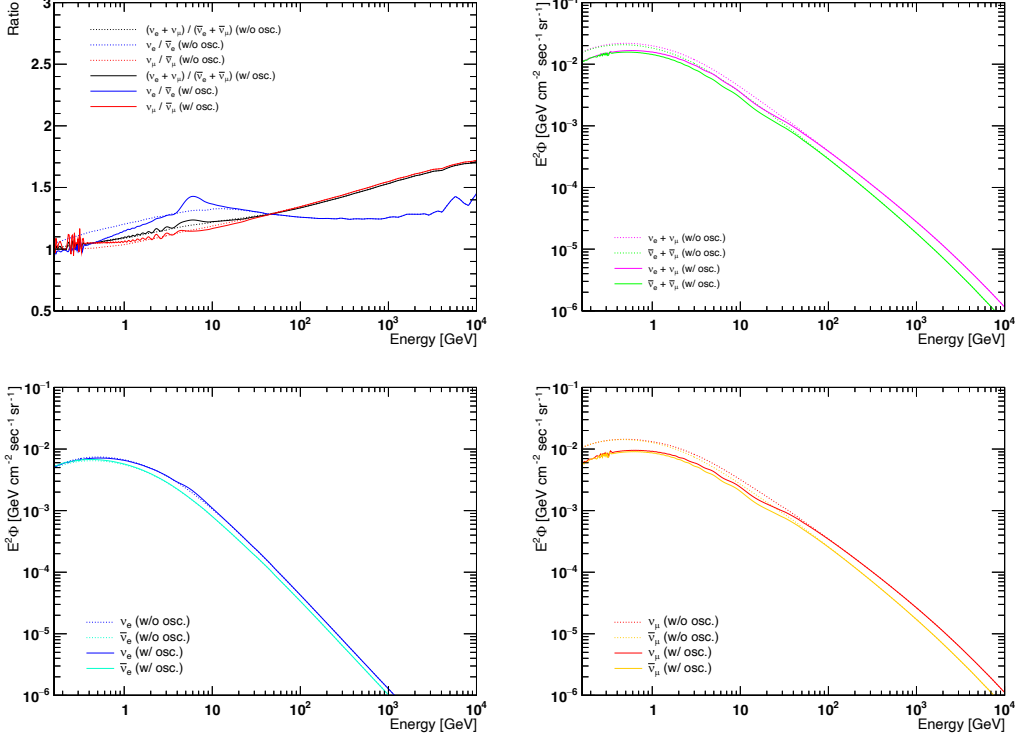


Figure 4.2: Atmospheric neutrino-antineutrino flux ratio predicted by the HKKM11 model for the Kamioka site (top left) [26]. Atmospheric neutrino fluxes of $\nu_e + \nu_\mu$ ($\bar{\nu}_e + \bar{\nu}_\mu$) (top right), ν_e ($\bar{\nu}_e$) (bottom left), and ν_μ ($\bar{\nu}_\mu$) (bottom right) are also shown.

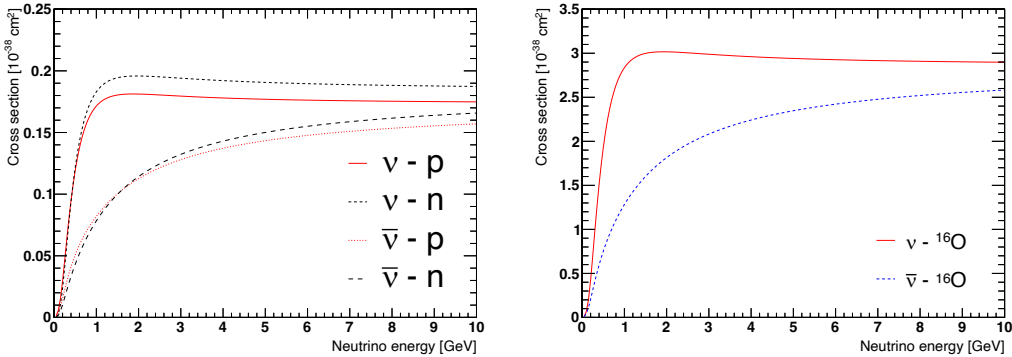


Figure 4.3: NCQE cross section on nucleon (left) and on oxygen nucleus (right) [28].

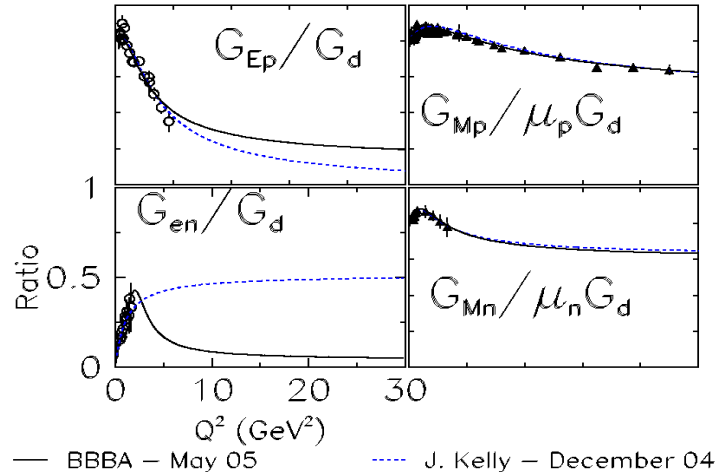


Figure 4.4: Ratio of the BBBA05 form factors to G_d (the dipole form factor) (shown in the solid black line) [29]. The dashed blue line shows the ratio of the Kelly form factors to G_d .

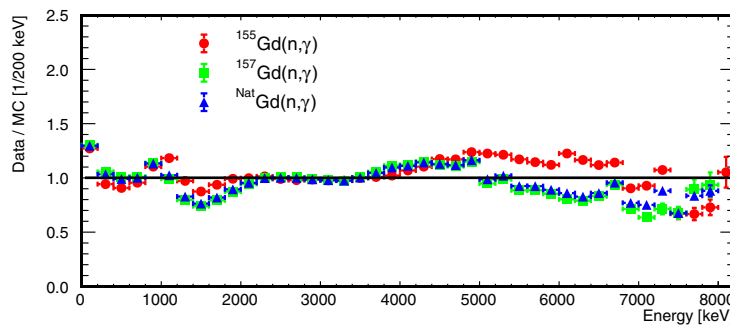


Figure 4.5: Ratio of data from the ANNRI experiment to MC with the ANNRI-Gd model for the single gamma-ray events [30].

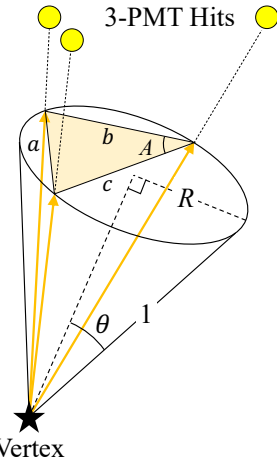


Figure 5.1: Schematic view of a cone and its angle defined by a combinations of 3-PMT hits.

5 Event reconstruction

5.1 Reconstructed Cherenkov angle of prompt signal

Reconstructed Cherenkov angle of prompt signal!

6 Event reduction

6.1 First reduction

First reduction!

6.2 Second reduction: spallation cut

Second reduction!

6.3 Third reduction

Third reduction!

6.4 Fourth reduction: neutron tagging

Fourth reduction!

7 Comparison of secondary interaction models

7.1 Secondary interaction models

Secondary interaction models!

8 NCQE cross section measurement

8.1 NCQE cross section measurement

NCQE cross section measurement!

9 Results

9.1 measured NCQE cross section

Measured NCQE cross section!

10 Conclusion

Conclusion!

A Neutrino oscillation between two neutrino species in vacuum

Here the neutrino oscillation between two neutrino species in vacuum is considered. The relationship between flavor eigenstates and mass eigenstates can be expressed as

$$\begin{pmatrix} |\nu_\alpha\rangle \\ |\nu_\beta\rangle \end{pmatrix} = \begin{pmatrix} \cos\theta & \sin\theta \\ -\sin\theta & \cos\theta \end{pmatrix} \begin{pmatrix} |\nu_1\rangle \\ |\nu_2\rangle \end{pmatrix} = \begin{pmatrix} \cos\theta|\nu_1\rangle + \sin\theta|\nu_2\rangle \\ -\sin\theta|\nu_1\rangle + \cos\theta|\nu_2\rangle \end{pmatrix}. \quad (\text{A.1})$$

From Equation (A.1),

$$\begin{pmatrix} |\nu_1\rangle \\ |\nu_2\rangle \end{pmatrix} = \begin{pmatrix} \cos\theta|\nu_\alpha\rangle - \sin\theta|\nu_\beta\rangle \\ \sin\theta|\nu_\alpha\rangle + \cos\theta|\nu_\beta\rangle \end{pmatrix}. \quad (\text{A.2})$$

References

- [1] “History of Neutrino”, <https://www-sk.icrr.u-tokyo.ac.jp/en/sk/neutrino/history/>.
- [2] J. Chadwick, Verh. Phys. Gesell. **16**, 383 (1914).
- [3] F. Reines, C. L. Cowan, Nature **178**, 446 (1956).
- [4] G. Danby *et al.*, Phys. Rev. Lett. **9**, 36 (1962).
- [5] K. Kodama *et al.*, Phys. Lett. B **504**, 218 (2001).
- [6] R. L. Workman *et al.*, Prog. Theor. Exp. Phys. **2022**, 083C01 (2022).
- [7] Y. Fukuda *et al.*, Phys. Rev. Lett. **81**, 1562 (1998).
- [8] T. K. Kuo, J. Pantaleone, Rev. Mod. Phys. **61**, 937 (1989).
- [9] “Particle Data Group”, <https://pdg.lbl.gov/> (2023).
- [10] K. Nakazato *et al.*, Astrophys. J. Suppl. **205**, 2 (2013).
- [11] K. S. Hirata *et al.*, Phys. Rev. D **38**, 448 (1988).
- [12] K. Abe *et al.*, Phys. Rev. D **104**, 122002 (2021).
- [13] G. L. Fogli *et al.*, J. Cosmol. Astropart. Phys. **2005**, 002 (2005).
- [14] M. Harada *et al.*, Astrophys. J. Lett. **951**, L27 (2023).
- [15] S. Fukuda *et al.*, Nucl. Instrum. Methods Phys. Res., Sect. A **501**, 418 (2003).
- [16] Z. Conner, “A STUDY OF SOLAR NEUTRINOS USING THE SUPER-KAMIOKANDE DETECTOR”, Ph.D. Thesis, University of Maryland (1997).
- [17] K. Abe *et al.*, Nucl. Instrum. Methods Phys. Res., Sect. A **737**, 253 (2014).
- [18] T. Yamaguchi, “Observation of ^8B Solar Neutrinos from 300-day data at Super-Kamiokande”, Ph.D. Thesis, University of Osaka (1998).
- [19] “Report from cause committee”, <https://www-sk.icrr.u-tokyo.ac.jp/cause-committee/> (2003).
- [20] H. Nishino *et al.*, Nucl. Instrum. Methods Phys. Res., Sect. A **610**, 710 (2009).
- [21] H. Watanabe *et al.*, Astropart. Phys. **31**, 320 (2009).
- [22] K. Abe *et al.*, Nucl. Instrum. Methods Phys. Res., Sect. A **1027**, 166248 (2022).
- [23] K. Yamamoto *et al.*, “Application of Cherenkov Light Observation to Reactor Measurements (1) - Estimation of Reactor Power from Cherenkov Light Intensity -”, JAEA-Technology 2014-028 (2015).
- [24] Y. Nakano, “ ^8B solar neutrino spectrum measurement using Super-Kamiokande IV”, Ph.D. Thesis, University of Tokyo (2015).

- [25] S. Yamada *et al.*, IEEE Trans. Nucl. Sci. **57**, 428 (2010).
- [26] M. Honda *et al.*, Phys. Rev. D **83**, 123001 (2011).
- [27] E. Richard *et al.*, Phys. Rev. D **94**, 052001 (2016).
- [28] A. M. Ankowski *et al.*, Phys. Rev. Lett. **108**, 052505 (2012).
- [29] R. Bradford *et al.*, Nucl. Phys. B, Proc. Suppl. **159**, 127 (2006).
- [30] T. Tanaka *et al.*, Prog. Theor. Exp. Phys. **2020**, 043D02 (2020).